

Phase transitions of adsorbed fluids computed from multiple-histogram reweighting

WEI SHI^{1,2}, XIONGCE ZHAO¹ and J. KARL JOHNSON^{1,2*}

¹ Department of Chemical and Petroleum Engineering, University of Pittsburgh,
Pittsburgh, PA 15261, USA

² National Energy Technology Laboratory, Pittsburgh, PA 15236, USA

(Received 15 August 2001; accepted 7 December 2001)

This paper demonstrates the effectiveness of using multiple-histogram reweighting (MHR) to study phase transitions in confined fluids by examining capillary condensation, prewetting, and layering transitions for different systems. A comparison is made with previously published simulations, where available, to establish the accuracy of MHR as applied to inhomogeneous systems. Overlap between adjacent state points is assessed through single-histogram reweighting. Capillary condensation for methane adsorption in slit-like graphite pores exhibits 2D behaviour. Crossover of the effective exponent for the width of the coexistence curve from 2D Ising-like (1/8) further away from the critical point to mean-field (1/2) near the critical point is observed. The reduced critical temperature, the density and the effective value of the exponent for the model system are 0.77, 0.482, and 0.119, respectively, based on a fit to the simulation data. Prewetting transitions are observed for adsorption of Ar on solid CO₂ using model potentials. The wetting temperature is estimated based on the intersection of the prewetting and bulk vapour–liquid lines, and also by extrapolation to zero of the difference between the saturation and prewetting chemical potentials. The reduced wetting temperature is estimated to be around 0.69. The reduced prewetting critical temperature, calculated from the disappearance of the two peaks in the density probability distribution, is estimated to be 0.92. The monolayer to bilayer (1–2) transition for propane on graphite is computed over a range of temperatures. Results for the 1–2 layering transition computed from MHR from a small system are in good agreement with grand canonical Monte Carlo simulations for a much larger system.

1. Introduction

Confined fluids are known to exhibit a rich variety of phase transitions that are absent in bulk fluids [1–3]. Perhaps three of the most interesting phenomena are capillary condensation, prewetting transitions and layering transitions. Each of these transitions has been studied previously in some detail through the use of a variety of computer simulation techniques. Different simulation methods may be required to characterize these different phenomena. For example, grand potential or Gibbs ensemble calculations are needed to locate capillary condensation [4–6]. Prewetting transitions are often located by plotting the isotherms and density profiles from grand canonical Monte Carlo or isothermal–isobaric Monte Carlo simulations [7, 8]. Layering transitions have been observed from grand canonical Monte Carlo simulations coupled with grand potential calculations [5].

In this paper we demonstrate that multiple-histogram reweighting (MHR) [9–11] can be an accurate and efficient tool for studying phase transitions in confined fluids. The MHR method has been shown to be useful for studying the phase behaviour of bulk fluids [12–15], but has not been used widely for studying the properties of confined fluids.

Gelb and Gubbins applied the histogram reweighting technique to study the phase diagram of a simple binary liquid mixture in the semi-grand canonical ensemble [16]. They used single histogram reweighting to estimate the biasing potential needed for barrier crossing. Escobedo and de Pablo studied the secondary transition for a 12-6 Lennard-Jones fluid in a composite large sphere matrix with histogram reweighting analysis [17]. Recently, Potoff and Siepmann calculated the effect of branching on the fluid phase behaviour of alkane monolayers using histogram reweighting with the finite-size scaling technique [18].

Capillary condensation occurs when a fluid is strongly adsorbed in a micropore below the capillary condensation critical temperature. The transition is characterized

* Author for correspondence. e-mail: karlj@pitt.edu

by a gas condensing to a liquid-like state that entirely fills the pore space at a bulk pressure less than the saturation value [19, 20]. Typically, grand canonical Monte Carlo (GCMC) simulations are used to construct the adsorption isotherms for the prediction of capillary condensation. Peterson and Gubbins [4] calculated the grand potential through integration of isotherms and paths of constant chemical potential in order to compute the equilibrium chemical potential for capillary condensation. In a completely different approach, Hefelfinger *et al.* [21] used quenched molecular dynamics to study capillary condensation in cylindrical pores. The chemical potentials of the gas-like and liquid-like regions were computed from the potential distribution theorem for inhomogeneous fluids. Some prior knowledge of the phase behaviour is required to implement this approach, because the overall density must be chosen such that the system is in the unstable region when quenched. Panagiotopoulos extended the Gibbs ensemble Monte Carlo method for the prediction of adsorption and capillary condensation [6]. The coexistence densities of gas-like and liquid-like phases in equilibrium inside a pore can be obtained through a single pore-pore calculation. However, then a series of pore-fluid calculations is needed to construct the isotherm.

The existence of wetting transitions was first predicted in 1977 independently by Cahn [22] and Ebner and Saam [23]. It was predicted that a gas that weakly adsorbs onto a solid surface will exhibit non-wetting behaviour at low temperatures and may undergo a first-order transition to wetting behaviour at a higher temperature T_w . By non-wetting we mean that the thickness of a film adsorbed on a surface remains finite at all pressures below the saturation vapour pressure; by wetting we mean that the film thickness diverges as the saturation pressure is approached. Prewetting occurs when there is a first-order transition from a thin film to a thick film adsorbed on the surface. The prewetting transition terminates at the critical prewetting temperature [24, 25]. Finn and Monson were the first to observe the existence of a prewetting transition through molecular simulation [8]. They used isothermal-isobaric Monte Carlo to identify the prewetting transition by observing the jump in adsorption on an isotherm associated with the thin-to-thick film transition [8]. Large fluctuations in the coverage typically accompany prewetting transitions, making precise location of the transition a difficult task. For this reason, later work by Fan and Monson [26] utilized calculation of the surface tensions in the thin and thick films in order to locate the prewetting transition more precisely. Experiments and simulations by Mistura *et al.* [27] demonstrated that Ar on solid CO₂ actually exhibits triple-point wetting, rather than prewetting as predicted by Monson and coworkers. The

reason for this discrepancy is that the potential models used in the simulations [8, 26] do not accurately represent the potential surface of the real Ar-CO₂ system. More realistic solid-fluid potential models [27] are more strongly attractive than the potential used by Monson *et al.* We note that grand canonical Monte Carlo simulations have been used to study prewetting transitions for a variety of other systems [28, 29].

Thick films adsorbing on a substrate can either grow continuously or in a stepwise fashion. If the growth is stepwise, then each layer grows by a succession of first-order layering transitions at pressures lower than the bulk saturation pressure [30]. Layering transitions of simple fluids and lower alkanes on graphite have been studied extensively through experimental techniques [31]. Iwamatsu has shown that layering transitions can be expected to occur for systems that exhibit both incomplete and complete wetting [32]. For wetting growth the thickness of the film increases to infinity as the bulk saturation pressure is approached. If the wetting is incomplete then a transition from incomplete wetting to wetting will occur as the temperature is increased. Layering transitions will persist to T_w if $T_w < T_R$ where T_R is the bulk roughening transition [33]. If $T_w > T_R$ then a thin-to-thick film prewetting transition precedes divergence of the film thickness. Each of the layers terminates at a layer critical point temperature, $T_c(m)$, where m is the number of layers in the film. It has been found that $T_c(m)$ can approach the triple point either from above [33] or below [34] with increasing m .

In this paper we demonstrate that MHR can be applied accurately and efficiently to compute capillary condensation, prewetting transitions, and layering transitions. Histograms for a given system can be combined in order to compute isotherms under any of the conditions spanned by the simulations. The location of phase transitions can be computed accurately through the equal area criterion [35] without resorting to computation of the grand potential [4, 5]. The precision of MHR allows us to observe crossover in the critical exponents for capillary condensation. This is difficult to accomplish through a series of isolated simulations. In this paper, we use MHR to construct estimates for the capillary condensation, wetting temperature and prewetting critical temperatures, and to find layering transition pressures for propane on graphite.

2. Theory and methods

The basic idea of MHR is that histograms collected from a number of independent simulations may be combined to construct an estimate for the partition function [9–11]. The multiple histogram reweighting technique can be used to calculate phase diagrams of bulk fluids

accurately [12–15, 35]. This method allows the calculation of equilibrium properties over a range of conditions from a relatively small number of state points. The phase diagrams from histogram reweighting can be very accurate [13]. The coexistence densities and saturation chemical potential can be calculated through the use of the equal area criterion and Hill’s method [35].

Sufficient overlap between histograms of adjacent state points is necessary in order to implement the MHR technique. Here we describe one method for checking for the extent of overlap between pairs of state points. The grand canonical partition function can be written as

$$\begin{aligned}\Xi(\mu, V, T) &= \sum_N \sum_{U_N} \exp[N\beta\mu - \beta U_N] \Omega(N, V, U_N) \\ &= \sum_N \sum_{U_N} CH(U_N, N),\end{aligned}\quad (1)$$

where $\beta = 1/kT$, k is the Boltzmann constant, T is the absolute temperature, $\Omega(N, V, U_N)$ is the microcanonical partition function, C is a simulation-specific constant, and $H(U_N, N)$ is the 2-dimensional histogram of configurational energy U_N and number of molecules N collected during the simulation. The configurational chemical potential μ is defined by

$$\mu = \mu^f - kT \ln \Lambda^3 + kT \ln(q_{\text{int}}), \quad (2)$$

where μ^f is the full chemical potential, Λ is the thermal de Broglie wavelength, and q_{int} is the intramolecular partition function, accounting for density independent terms such as rotational and vibrational Hamiltonians. The grand canonical partition function for a different state point with configurational chemical potential μ' and temperature T' can be estimated by single-histogram reweighting:

$$\begin{aligned}\Xi(\mu', V, T') &= \sum_N \sum_{U_N} \exp[N\beta'\mu' - \beta' U_N] \Omega(N, V, U_N) \\ &= \sum_N \sum_{U_N} \exp[N(\beta'\mu' - \beta\mu) - (\beta' - \beta)U_N] \\ &\quad \times H_{\mu, V, T}(U_N, N)C,\end{aligned}\quad (3)$$

where $H_{\mu, V, T}(U_N, N)$ is the histogram collected at (μ, V, T) . The ratio of the grand canonical partition functions between these two state points based on the histogram collected at (μ, V, T) is computed through

$$\frac{\Xi(\mu', V, T')}{\Xi(\mu, V, T)} = \frac{\sum_N \sum_{U_N} \exp[N(\beta'\mu' - \beta\mu) - (\beta' - \beta)U_N] H_{\mu, V, T}(U_N, N)}{\sum_N \sum_{U_N} H_{\mu, V, T}(U_N, N)}.\quad (4)$$

Likewise, one may collect histogram data at the state point defined by (μ', V, T') and extrapolate to

(μ, V, T) . The ratio of these two partition functions can be expressed by interchanging μ with μ' and T with T' in equation (4). In the thermodynamic limit the following equation must be satisfied:

$$\frac{\Xi(\mu', V, T')}{\Xi(\mu, V, T)} \times \frac{\Xi(\mu, V, T)}{\Xi(\mu', V, T')} = 1. \quad (5)$$

We use equation (5) to check the extent of overlap between histograms by performing relatively short GCMC simulations at each state point. Not all of the fluctuations in energy and particle number accessible to the state points in the thermodynamic limit can be observed in a finite simulation. Consequently, equation (5) will not be satisfied exactly for state points extrapolated from histogram reweighting, but should be satisfied approximately within some tolerance

$$\left. \frac{\Xi(\mu', V, T')}{\Xi(\mu, V, T)} \right|_{\text{HR}} \times \left. \frac{\Xi(\mu, V, T)}{\Xi(\mu', V, T')} \right|_{\text{HR}} = 1 \pm \delta, \quad (6)$$

where the subscript HR indicates that the partition function in the numerator has been extrapolated from histogram reweighting. We have found that $\delta = 0.65$, that is, values of the LHS of equation (6) between 0.35 and 1.65 indicate sufficient overlap of the two state points. We have used this method to select the state points to simulate in longer production runs. We denote this procedure to check the overlap as the single-histogram reweighting method (SHR). Note that equation (6) is not symmetric with respect to inversion because we stipulate that the extrapolated partition functions are always in the numerator.

Details of our implementation of the multiple-histogram reweighting technique are described elsewhere [35]. The ratios of the Ξ s for several state points were obtained from multiple-histogram reweighting and compared with the values calculated from equation (4) in order to verify that the degree of overlap between adjacent state points was sufficient. Single-histogram reweighting from equation (6) and MHR were used to analyse the histograms. The results are presented in table 1. The values computed from MHR are based on a combination of 30 histograms. The values of the ratios Ξ_2/Ξ_1 between 10 pairs of state points as calculated from SHR and MHR are tabulated in table 1. The good agreement between the two methods indicates that a value of $\delta \leq 0.65$ in equation (6) is indicative of histograms with sufficient overlap.

3. Capillary condensation

In this section we present results of MHR for capillary condensation. The potential model used to investigate capillary condensation is the same as that used by

Table 1. Ratios of the grand canonical partition function computed from single-histogram reweighting (SHR) and multiple-histogram reweighting (MHR). The calculation is for methane adsorption in graphitic slit pore.

T_1^*	μ_1^*	T_2^*	μ_2^*	SHR			MHR
				$\frac{\Xi_1}{\Xi_2}$	$\frac{\Xi_2}{\Xi_1}$	$\frac{\Xi_1}{\Xi_2} \times \frac{\Xi_2}{\Xi_1}$	$\frac{\Xi_2}{\Xi_1}$
0.9	-5.57	0.9	-5.50	7.5374×10^{-14}	1.5222×10^{13}	1.1473	1.4971×10^{13}
0.9	-5.50	0.9	-5.45	3.7830×10^{-11}	2.9184×10^{10}	1.1040	2.7088×10^{10}
0.9	-5.45	0.9	-5.40	6.9859×10^{-12}	1.352×10^{11}	0.9444	1.3634×10^{11}
0.85	-5.65	0.9	-5.57	7.5537×10^{27}	1.3189×10^{-28}	0.9962	1.2211×10^{-28}
0.75	-5.90	0.7	-6.10	2.5573×10^{-26}	1.6060×10^{25}	0.4107	3.3113×10^{25}
0.7	-6.6	0.7	-7.0	3.7151×10^{71}	2.7838×10^{-72}	1.0342	2.7188×10^{-72}
0.65	-7.2	0.6	-7.6	2.4925×10^{17}	4.0865×10^{-18}	1.0185	4.4315×10^{-18}
0.9	-5.0	0.85	-5.0	1.1024×10^{-65}	1.4597×10^{65}	1.6091	1.1898×10^{65}
0.725	-5.90	0.725	-5.8	1.8069×10^{-34}	8.9568×10^{33}	1.6184	6.8511×10^{33}
0.7	-5.9	0.685	-6.02	1.8520×10^{14}	4.9617×10^{-15}	0.9189	4.5241×10^{-15}

Jiang *et al.* [5], namely, methane adsorbing in a graphite slit-like pore of width $H = 5\sigma$, where σ is the Lennard-Jones (LJ) diameter of a methane molecule. The fluid particles in the slit pore interact with each other via the truncated and shifted (TS) LJ potential

$$\phi_{\text{TS}}(r) = \begin{cases} \phi(r) - \phi(r_c) & r \leq r_c, \\ 0 & r > r_c, \end{cases} \quad (7)$$

where $\phi(r)$ is the full LJ potential given by

$$\phi(r) = 4\epsilon \left[\left(\frac{\sigma}{r} \right)^{12} - \left(\frac{\sigma}{r} \right)^6 \right], \quad (8)$$

ϵ is the well depth and σ is the molecular diameter. The value of the cutoff was 2.5σ , as used in [5]. The solid-fluid interactions are represented by the 10-4-3 solid-fluid potential [36, 37]

$$\phi_{\text{sf}}(z) = 2\pi\rho_s\epsilon_{\text{sf}}\sigma_{\text{sf}}^2\Delta \left[\frac{2}{5} \left(\frac{\sigma_{\text{sf}}}{z} \right)^{10} - \left(\frac{\sigma_{\text{sf}}}{z} \right)^4 - \left(\frac{\sigma_{\text{sf}}^4}{3\Delta(0.61\Delta + z)^3} \right) \right], \quad (9)$$

where z is the distance between a fluid particle and a solid surface, Δ is the separation between the individual graphene planes, and ρ_s is the solid density. The cross-parameters σ_{sf} and ϵ_{sf} were calculated from the Lorentz-Berthelot combining rules. The parameters were taken from [36, 37]: they are $\sigma_{\text{ff}} = 0.381$ nm, $\epsilon_{\text{ff}}/k = 148.1$ K, $\sigma_{\text{ss}} = 0.340$ nm, $\epsilon_{\text{ss}}/k = 28.0$ K, $\Delta = 0.335$ nm, and $\rho_s = 114$ nm⁻³. For a given slit pore of width H , the external potential experienced by a fluid molecule at z is given by $\phi_{\text{ext}}(z) = \phi_{\text{sf}}(z) + \phi_{\text{sf}}(H - z)$.

The volume of the unit cell was fixed at $900\sigma^3$ with a separation of 5σ between the two opposite adsorbent surfaces. The lateral dimensions of the box were equal

in the x and y directions. Periodic boundary conditions in the x and y directions were employed. We used 7×10^7 trials to achieve equilibrium and 7×10^7 moves for data collection. Histograms were collected every 14 moves. Standard reduced units were used, with the reduced temperature given by $T^* = kT/\epsilon$ and the reduced density $\rho^* = \rho\sigma^3$. The reduced chemical potential is $\mu^* = \mu/\epsilon$.

We combined 30 histograms in the reduced temperature region from 0.6 to 0.9. Two representative isotherms are plotted in figure 1. As a general test of the accuracy of the MHR isotherms we have also plotted

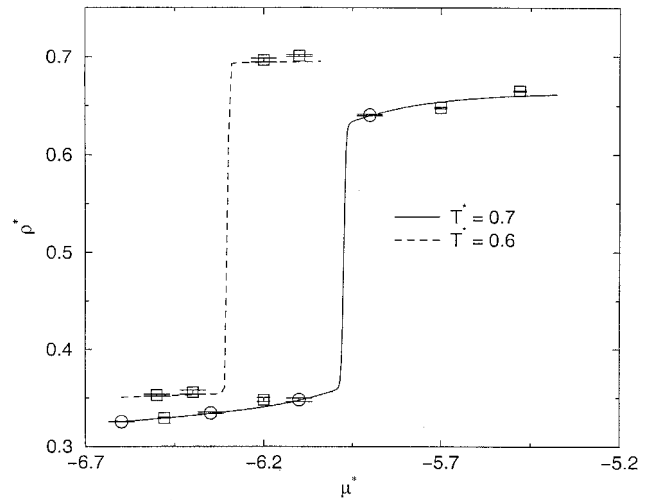


Figure 1. Isotherms for $T^* = 0.7$ (solid line) and 0.6 (dashed line) from multiple histogram reweighting for methane adsorption in a graphitic slit pore of width 5σ . Data from individual GCMC simulations that were not included in the MHR calculations are shown.

state points calculated directly from GCMC simulations in figure 1. We present data from simulations that were included in generating MHR isotherms and also data from state points that were not used to construct the histograms in the MHR. The differences between densities obtained from multiple-histogram reweighting and those from GCMC simulations are small. The average densities obtained from 19 GCMC simulations not included in multiple-histogram reweighting were compared with densities from multiple-histogram reweighting. The isotherms examined were $T^* = 0.9, 0.85, 0.825, 0.8, 0.7$, and 0.6 . The average absolute error in the densities between GCMC and MHR is 3×10^{-3} . The maximum and minimum absolute errors are 7×10^{-3} and 2×10^{-4} , respectively. Many of the values from MHR agree with those from the simulations, within the uncertainty of the simulations.

For $T^* = 0.7$, the values of the coexistence densities computed from MHR are 0.358 and 0.631 for the vapour-like and liquid-like branches, respectively, and the capillary condensation coexistence chemical potential μ_{cc}^* is -5.978 . These data are in excellent agreement with the values from Jiang *et al.* [5], who reported densities of 0.36 and 0.627 for the vapour-like and liquid-like branches, respectively, and $\mu_{cc}^* = -5.93$. Jiang *et al.* located the coexistence points by calculating the grand potentials in each branch. The equilibrium transition occurs when the grand potentials in each phase are equal [4], whereas adsorption and desorption isotherms are plagued by metastability-induced hysteresis.

The lowest temperatures where histograms were collected were 0.6 and 0.65 for the vapour-like and liquid-like sides, respectively. The $T^* = 0.6$ isotherm was generated by extrapolating the histograms at higher temperatures and lower densities in order to generate the liquid-like branch of the isotherms. This is possible because fluctuations recorded at higher temperatures and lower densities sample some of the microstates important at lower temperatures and higher densities, giving a physically realistic extrapolation. The reliability of the extrapolation is confirmed by the agreement between the MHR isotherm and the two simulation points (not included in the histograms) on the liquid-like branch shown in figure 1. The values of coexistence densities from MHR are 0.360 and 0.692 for the vapour-like and liquid-like branches, respectively. These values are very close to those of 0.36 and 0.68 from Jiang *et al.* [5]. The MHR isotherm gives $\mu_{cc}^* = -6.309$, which is in good agreement with the value computed from grand potential calculations of -6.32 [5].

The coexistence densities in the reduced temperature region from 0.68 to 0.76 were fitted to the scaling law and rectilinear law [38]:

$$\frac{\rho_l^* + \rho_v^*}{2} = \rho_c^* + A(T^* - T_c^*), \quad (10)$$

$$\rho_l^* - \rho_v^* = B(T_c^* - T^*)^{\beta_c}, \quad (11)$$

where ρ_l^* and ρ_v^* are the reduced coexistence densities for the liquid-like and vapour-like branches, respectively, T_c^* and ρ_c^* are the reduced critical temperature and density, β_c is the critical exponent, and A and B are fitting parameters. Regression of the MHR equilibrium data to equations (10) and (11) gave $T_c^* = 0.77$, $\rho_c^* = 0.482$, and $\beta_c = 0.119$. The fitted value of β_c is reasonably close to the value of 0.125 (1/8) for the 2D Ising universality class [39]. The data calculated from MHR and the fitting are shown in figure 2.

The crossover of the effective exponent from 2D Ising-like (1/8) away from the critical point to the mean-field value (1/2) in the immediate vicinity of the critical point is clear in figure 3. These results reveal the 2D behaviour of capillary condensation. As Mon and Binder have pointed out [40], one expects the observed exponents to correspond to the correct universality class when the correlation length is much less than the simulation box length. This is indeed the case for low temperatures, corresponding to $T^* < 0.74$ for the system represented in figure 3. At temperatures near the capillary condensation critical point the correlation length becomes large compared with the box length, and the fluid then conforms to mean field behaviour due to the suppression of critical fluctuations. Figure 3 is, to

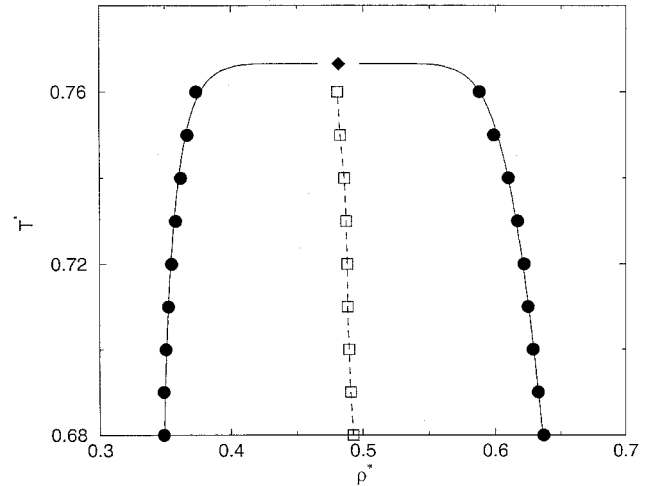


Figure 2. T^* versus ρ^* phase diagram for capillary condensation of methane in a graphitic slit pore. The filled circles are the coexistence data calculated from the equal area criterion. The filled diamond is the critical point estimated from fitting the coexistence data to the rectilinear and scaling laws, equations (10) and (11). The solid line is the fit to the data. The squares are the rectilinear diameters. The dashed line is provided as a guide to the eye.

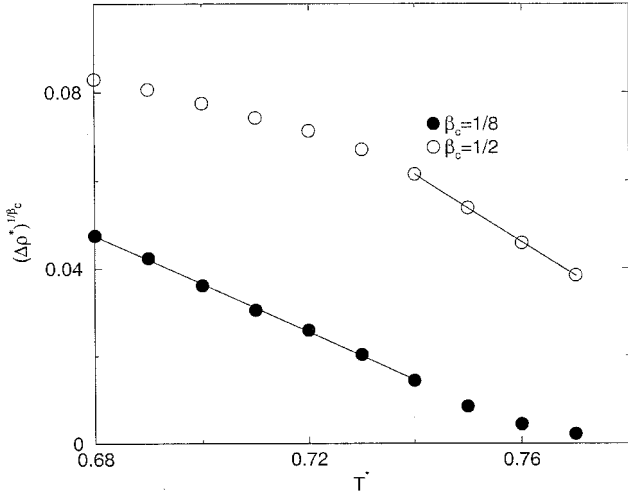


Figure 3. Scaled width of the coexistence data versus reduced temperatures for the capillary condensation of methane in a graphitic slit pore. The 2D Ising exponent of $\beta_c = 1/8$ is shown as \bullet and \circ denotes the mean-field value of $\beta_c = 1/2$.

the best of our knowledge, the first observation of cross-over for capillary condensation.

4. Prewetting

In this section we present details and results of our MHR calculations for a system that exhibits a prewetting transition. We have investigated the same system as studied by Monson and coworkers, namely, Ar adsorbing on a solid CO_2 surface [8, 26, 41]. Their simulations were performed for a fluid interacting through the truncated LJ potential,

$$\phi_{\text{TR}}(r) = \begin{cases} \phi(r) & r \leq r_c, \\ 0 & r > r_c, \end{cases} \quad (12)$$

where $\phi(r)$ is the full LJ potential given by equation (8) and r_c is 2.5σ . The fluid–solid interaction at the adsorbing wall is given by the LJ 9-3 potential,

$$\phi_w(z) = \frac{2\pi}{3} \rho_w \sigma_w^3 \varepsilon_w \left[\frac{2}{15} \left(\frac{\sigma_w}{z} \right)^9 - \left(\frac{\sigma_w}{z} \right)^3 \right], \quad (13)$$

with $\sigma_w = 0.3727$ nm, $\varepsilon_w/k = 153$ K, $\rho_w \sigma_w^3 = 0.988$, and z is the distance between the fluid and the adsorbing wall. The opposite wall was chosen to be reflecting. The parameters for the fluid–fluid interactions are $\varepsilon/k = 119.8$ K, and $\sigma = 0.340$ nm.

Monson and coworkers [8, 26, 41] reported isotherms between $T^* = 0.83$ and 1.0 for pressures up to saturation. Their estimate for the reduced wetting temperature is $T_w^* = 0.84 \pm 0.01$, and the reduced prewetting critical temperature estimate is $T_{\text{pwc}}^* = 0.94 \pm 0.02$. They observed a prewetting transition at $T^* = 0.88$ from

their simulations, but no prewetting transitions at $T^* = 0.83$ and $T^* = 0.80$.

In this work we have chosen the volume of the unit cell for the Ar/ CO_2 model system to be $1620\sigma^3$ with $H = 20\sigma$. Periodic boundary conditions were applied in the x and y directions. We used 10^7 steps for equilibration followed by an additional 10^8 steps for data collection. Histograms were collected at every step. We collected and combined 30 histograms in the temperature region from 0.8 to 1.05. We compute the total, not excess adsorption in this work. Note that the equal area criterion can be used with the total adsorption to find prewetting transitions. The bulk density term adds a constant to both the thin and thick films at a fixed T^* and μ^* . This constant cancels out when computing the difference between the areas of the probability density distributions. The ability to use total instead of excess adsorption isotherms is an advantage because the procedure for computing excess adsorption in a simulation is somewhat ambiguous [42–44].

Several isotherms computed from MHR are shown in figure 4, along with results from GCMC simulations. The differences between densities obtained from GCMC simulations and MHR are typically smaller than the errors in the simulations. Prewetting is associated with the first S shaped rise in coverage in figure 4 for $T^* = 0.83$ and 0.88. The second rise and plateau are associated with box filling close to the bulk saturation point. The prewetting transition exhibits considerable rounding due to finite-size effects [45]; hence it is difficult to tell if there is a first-order transition from the shape of the isotherm. The coexistence densities and chemical

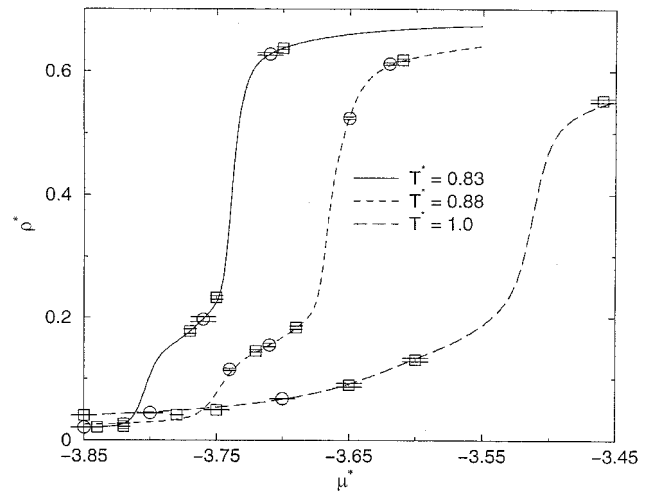


Figure 4. Isotherms for $T^* = 0.83$ (solid line), 0.88 (dashed line), and 1.0 (long dashed line) from multiple histogram reweighting for Ar adsorption on solid CO_2 . Data from individual GCMC simulations that were (\circ) and were not (\square) included in the MHR calculations are shown.

potentials were computed from the equal area criterion, as for capillary condensation. Hill's method was used to get an initial estimate for the value of the coexistence chemical potential [35]. The existence of two distinct peaks with equal areas in the density probability is sufficient to identify the transition as first order. The density probability distribution at $T^* = 0.83$ and $\mu^* = -3.801$ is shown in figure 5. We also obtained a two peak equal area density distribution for $T^* = 0.80$. This is significant because Monson and coworkers did not observe prewetting transitions at these temperatures. At these low temperatures, the prewetting transition pressure is closer to the saturation pressure than at higher temperatures, making identification of the prewetting transition especially difficult from standard simulations. However, MHR allows relatively easy identification of prewetting transitions, even very near the saturation pressure.

The prewetting transitions seen on the $T^* = 0.83$ and 0.88 isotherms can also be characterized by the local density profiles, shown in figures 6 and 7. We note that density profiles cannot be computed from MHR because we have not collected histograms of $\rho(z)$ as a function of U_N, N . Referring to figure 6, we observe that adsorption is limited to a thin layer on the surface for $\mu^* < -3.8$. For $\mu^* \geq -3.8$ the adsorption changes abruptly to multiple layers that appear to grow continuously as the chemical potential is increased. This behaviour is indicative of a prewetting transition occurring. The coexistence chemical potential at this temperature calculated from the equal area criterion is -3.801 , in agreement with the local density profiles in figure 6. Similar behaviour can be seen in figure 7, where the thin-to-thick film transition occurs between $\mu^* = -3.76$ and -3.75 . The coexistence chemical potential calculated from MHR is about -3.75 , in agreement with the local density profiles.

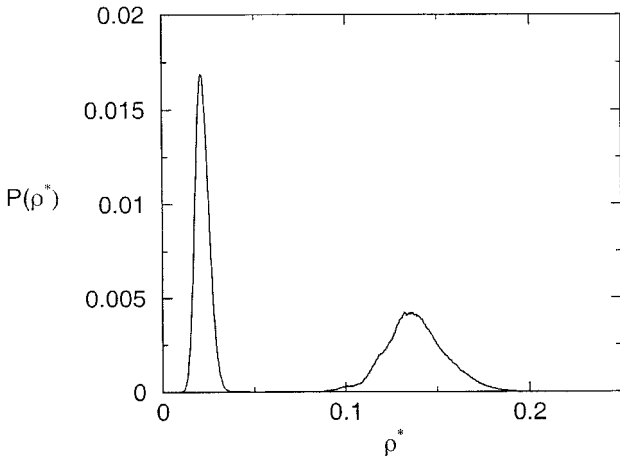


Figure 5. Density probability distribution for the same system as in figure 4 for $T^* = 0.83$ and $\mu^* = -3.801$.

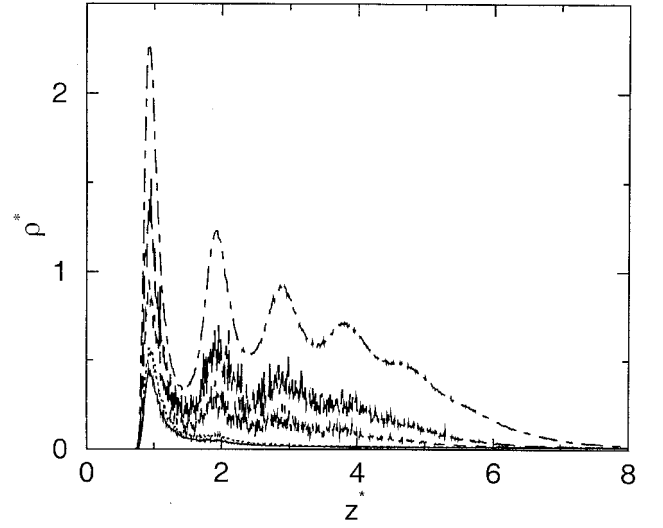


Figure 6. Local density profiles obtained from GCMC simulations for the same system as in figure 4. Profiles are for $\mu^* = -3.9$ (solid line), -3.81 (dotted line), -3.8 (dashed line), -3.78 (long dashed line), and -3.77 (dot-dashed line) at $T^* = 0.83$.

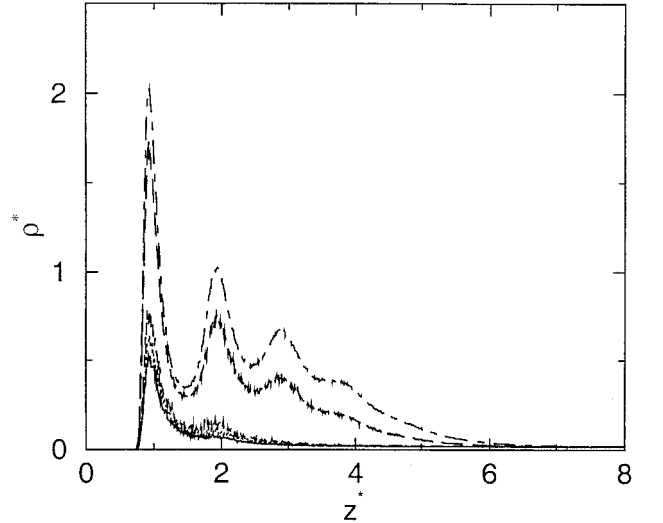


Figure 7. Local density profiles obtained from GCMC simulations for the same system as figure 4. Profiles are for $\mu^* = -3.85$ (solid line), -3.8 (dotted line), -3.76 (dashed line), -3.75 (long dashed line), and -3.73 (dot-dashed line) at $T^* = 0.88$.

We have computed the saturation chemical potential (μ_{sat}^*) for the bulk phase vapour-liquid transition from $T^* = 0.8$ up to the apparent critical point from MHR of the bulk fluid [35]. The values of the prewetting transition chemical potentials (μ_{pw}^*) were computed over $0.8 \leq T^* \leq 0.88$ from which $\Delta\mu^* = \mu_{\text{sat}}^* - \mu_{\text{pw}}^*$ was computed. The plot of $\Delta\mu^*$ versus T^* is shown in figure 8. Theoretical predictions indicate that $\Delta\mu^* \propto (T^* - T_w^*)^{3/2}$

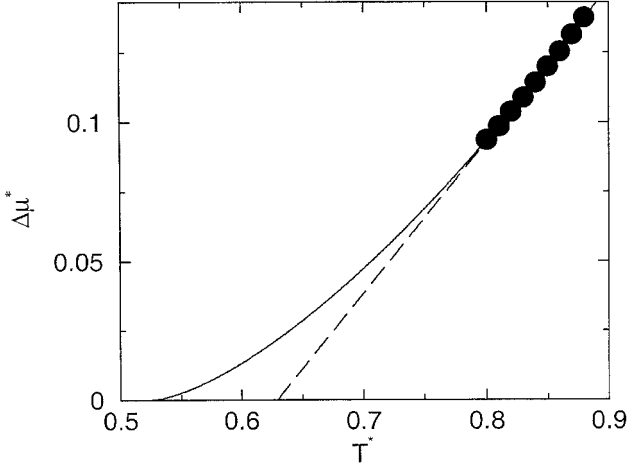


Figure 8. $\Delta\mu^* = \mu_{\text{sat}}^* - \mu_{\text{pw}}^*$ as a function of temperature for the same system as in figure 4. Filled circles are computed from MHR. Also shown are the fits to the data to the power law form (solid line), and linear form (long dashed line).

[46]. Hence, a plot of $\Delta\mu^*$ versus T^* can be used to identify the wetting temperature by extrapolating the curve to $\Delta\mu^* = 0$ [47]. The solid line in figure 8 is the result of a power law fit to the data using an exponent of $3/2$. However, an inspection of the simulation data reveals that they lie on a straight line with a correlation coefficient of 0.9994. The estimates of T_w^* from the power law and linear fits are 0.53 and 0.623, respectively.

The prewetting line for this system was computed [48, 49] in order to compare with data from [8]. The density of the gas in equilibrium with the adsorbed phase at the prewetting point was computed by

$$\rho_{\text{pw}}^* = \rho_{\text{sat}}^* \exp\left(\frac{\mu_{\text{pw}}^* - \mu_{\text{sat}}^*}{T^*}\right), \quad (14)$$

where ρ_{pw}^* and ρ_{sat}^* are the reduced bulk densities for gas at the prewetting transition and vapour–liquid saturation, respectively. This assumes that the bulk gas is ideal in the calculation. The results are shown in figure 9. The prewetting transition densities at $T^* = 0.85, 0.87$ and 0.88 are 0.0146, 0.0170 and 0.0183, respectively. These results agree well with values reported by Finn and Monson [8]. We fitted the prewetting line and the saturated vapour line to two separate polynomials. The solid and long dashed lines are the results from the fitting. The value of T_w^* was estimated by extrapolating the two lines to where they intersect. This gave $T_w^* = 0.69$. We note that it has been predicted from theory that the prewetting and bulk saturation lines should meet tangentially [8, 48–50]. Therefore, extrapolation of the two polynomials is not only unreliable but also theoretically not justified. Nevertheless, the estimate of $T_w^* = 0.69$ is

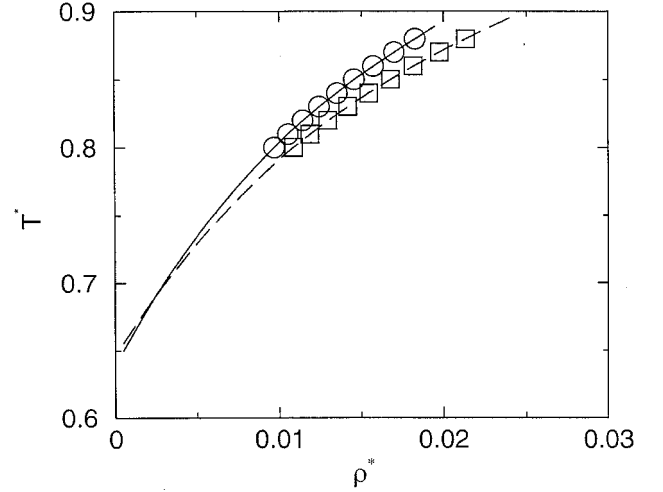


Figure 9. Temperature–density phase diagram for the same system as in figure 4. The circles are the densities of the bulk gas in equilibrium with the adsorbed fluid at the prewetting transition points calculated from MHR. The squares are the vapour side of the bulk vapour–liquid phase diagram computed from MHR of the bulk fluid. The solid line and the dashed line are polynomial fits to the data. The two lines intersect at $T^* = 0.69$.

in reasonable agreement with $T_w^* = 0.62$ obtained from linear extrapolation of $\Delta\mu^*$ versus T^* .

The reduced wetting and critical prewetting temperatures estimated for the Ar/CO₂ system or similar systems are given in table 2. Note that many of the calculations employed density functional theory, which is not expected to give results identical to simulations given the approximations in the theory. From a comparison with the previous estimates of T_w^* we conclude that the power law extrapolation of the $\Delta\mu^*$ versus T^* curve is not accurate. We believe that T_w^* for this system is probably close to our estimates from linear $\Delta\mu^*$ versus T^* extrapolation and extrapolation of the prewetting line, $T_w^* \sim 0.69$. The estimate by Finn and Monson of $T_w^* = 0.84$ is undoubtedly too high, given that we definitely observe a prewetting transition at $T^* = 0.8$.

Table 2. Reduced wetting temperature T_w^* and reduced prewetting critical temperature T_{pwc}^* for Ar on CO₂ and Ne on Mg

Source	T_w^*	T_{pwc}^*
Ebner and Saam [23]	0.77	0.92
Tarazona and Evans [60]	0.957	0.988
Meister and Kroll [61]	0.90	—
Finn and Monson [8]	0.84 ± 0.01	0.94 ± 0.02
Sokołowski and Fischer [62]	0.975 ± 0.025	—
Bojan <i>et al.</i> [63]	0.65	0.88 ± 0.03
This work	0.69	0.92

The relative ratios $P_{\text{wet}}/P_{\text{sat}}$ are plotted in figure 10. The ratio was computed from $P_{\text{wet}}/P_{\text{sat}} = \exp((\mu_{\text{pw}}^* - \mu_{\text{sat}}^*)/T^*)$, where P_{wet} and P_{sat} are the pressures at the prewetting transition and saturation, μ_{pw}^* and μ_{sat}^* are the reduced chemical potentials calculated from MHR with the equal area criterion. Ideal gas behaviour was assumed in the calculation. As expected, the ratio decreases with temperature. The value at $T = 0.88$ is 85.5%, close to 87.9% calculated by Finn and Monson [8].

The density probability distributions at $T^* = 0.92$ for $-3.72 \leq \mu^* \leq -3.66$ are shown in figure 11(a). The

isotherm is shown in figure 11(b). It is difficult to tell from the isotherm whether or not there is a prewetting transition at this temperature (figure 11(b)). However, the density probability distributions are definitive proof that $T^* = 0.92$ is above the prewetting critical point, because the equal area criterion cannot be satisfied for any choice of μ^* (figure 11(a)). Probability distributions at $T^* = 0.91$ and 0.9 are somewhat ambiguous. They show two peaks that are in the process of merging. From these observations we estimate that T_{pwc}^* is close to 0.92. This value is in reasonable agreement with other estimates (see table 2). We note that an accurate estimate of T_{pwc}^* would require a finite-size scaling analysis, which is beyond the scope of this work.

5. Layering transitions

In this section we present our MHR predictions for the 1–2 layering transition of propane on the basal plane of graphite. Propane was modelled as a three-site united atom molecule using the potential model of Lustig and Steele [51]. The potential parameters for this model are the LJ parameters ε and σ , the bond lengths of the isosceles triangular framework δ , and the bond angle θ . The values of the potential parameters are $\varepsilon/k = 119.57$ K, $\sigma = 3.527$ Å, $\delta = 2.16$ Å, and $\theta = 90^\circ$. There are several united atom propane models available in the literature [52–55]. We adopted this model because of its accuracy in predicting the PVT properties and internal energies of pure propane and the good agreement between experimental and simulated adsorption isotherms for propane on graphite [56]. The graphite surface was modelled as a smooth basal plane using the 10-4-3 potential given by equation (9).

The volume of the simulation box for histogram collection calculations was set to $1000\sigma^3$. Periodic boundary conditions and minimum image conventions were applied in the x and y directions of the simulation box. The lateral dimensions of the simulation box were equal in the x and y directions. One wall of the simulation box was chosen as the adsorbing surface and the opposite wall was chosen to be purely repulsive to keep the molecules in the box. The separation between the two walls was fixed at $H = 10\sigma$ so that the influence of the repulsive wall on the adsorption properties was negligible. The site–site interaction cutoff distance was 3.5σ and no long range corrections were applied. Each simulation was equilibrated for 5×10^7 moves, after which histogram data were collected for another 5×10^7 moves. We collected histograms spanning coverages ranging from a monolayer ($5.9 \mu\text{mol m}^{-2}$) to a complete bilayer ($14.2 \mu\text{mol m}^{-2}$) at a temperature of 130 K. We chose this temperature because it appears to be above the critical layering transition temperature, which allowed sampling of all coverages spanning the 1–2

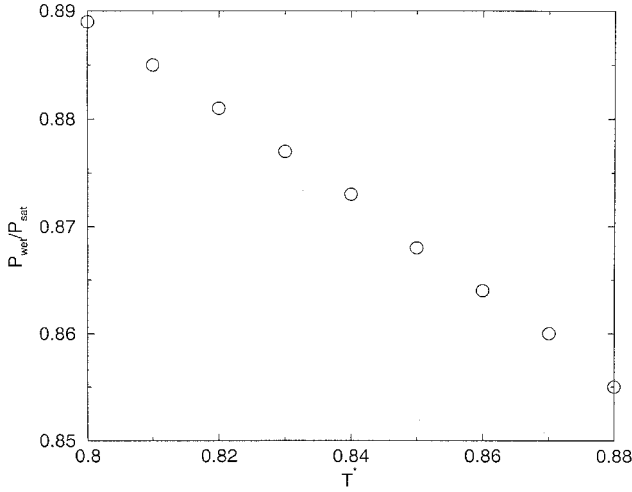


Figure 10. Ratio of the prewetting transition pressure to the saturation pressure for the same system as in figure 4.

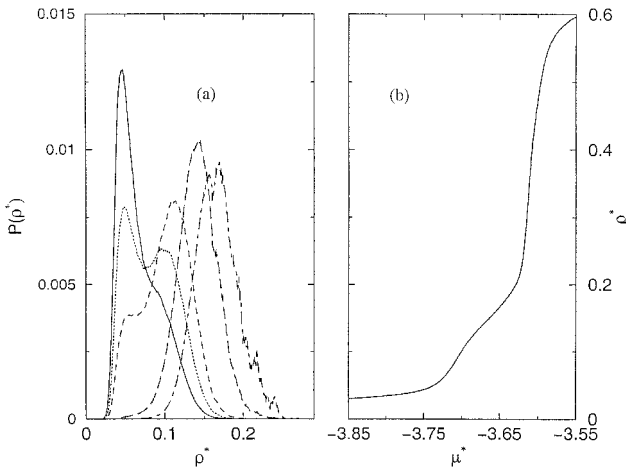


Figure 11. (a) Density probability distributions for the same system as in figure 4 at $T^* = 0.92$. Distributions are for chemical potentials of $\mu^* = -3.72$ (solid line), -3.71 (dotted line), -3.7 (dashed line), -3.67 (long dashed line) and -3.65 (dot-dashed line). (b) Isotherm computed from MHR at $T^* = 0.92$.

layering transition. Additional histograms were collected at temperatures down to 100 K, but only sampling a few state points in the monolayer or bilayer regime. A total of 53 histograms from different state points were collected.

An independent series of GCMC simulations was performed (without collecting histograms) for a larger system size with a volume of $4250\sigma^3$ and $H = 20\sigma$ [56]. The isotherms predicted from MHR for the smaller volume are compared with GCMC simulations in figures 12 and 13. We observe that the MHR calculations on the small system size give a very reasonable representation of the behaviour of the larger system size. The layering transitions occur at close to the same pressures, although there is some difference in the coverages, which may be due to finite-size effects. The 1–2 layering transition observed from the GCMC simulations does not appear to be very sharp. In contrast to simple fluids like methane on graphite [57], that show very sharp layering transitions, the propane–graphite system is complicated by orientational changes of the propane in the first layer. The orientational changes allow an increase in coverage in the first layer after the monolayer is apparently ‘full’ and also promotes adsorption in the second layer [56]. Density distributions from MHR at 100 K show two regions that are not well separated. This may be indicative of system size effects. We have previously observed that vapour–liquid density distributions for bulk fluids start to merge for subcritical temperatures, when the system size is small.

The value of the critical layering transition temperature is often of interest [31]. In principle, one can esti-

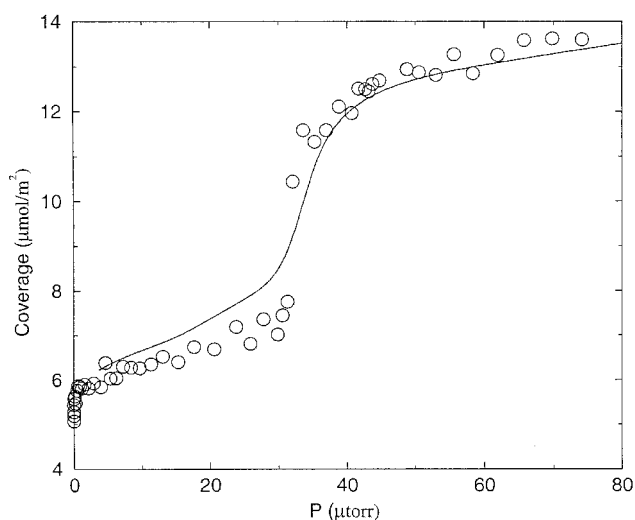


Figure 12. $T = 100$ K isotherm (solid line) for propane adsorption on graphite predicted from MHR for a small system size (volume = $1000\sigma^3$) compared with GCMC simulations for a larger system volume of $4250\sigma^3$ (circles).

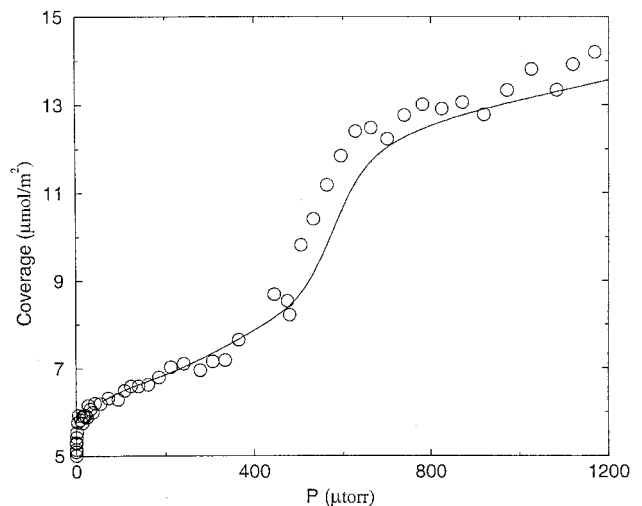


Figure 13. $T = 110$ K isotherm (solid line) for propane adsorption on graphite predicted from MHR for a small system size (volume = $1000\sigma^3$) compared with GCMC simulations for a larger system volume of $4250\sigma^3$ (circles).

mate the location of the critical layering transition temperature by the disappearance of two distinct peaks in the density distribution. However, the lack of distinct peaks is not a necessary condition for supercriticality, since two peaks in the density probability distribution may be observed for temperatures slightly greater than the apparent critical temperature [58]. A rigorous estimate of the critical layering transition temperature would require finite-size scaling analysis. An additional problem for this system is that the density distributions at subcritical temperatures are not well separated to begin with. Nevertheless, we have estimated $T_c(2)$ to be around 120 K for the propane–graphite system. This value is very close to the experimental result for ethane on graphite of $T_c(2) = 120.8 \pm 0.3$ K [59]. It is somewhat surprising that $T_c(2)$ is so similar for ethane and propane. This may be due to inaccuracies in the potential models used in these simulations, or perhaps due to the orientational transitions in the propane monolayer. Additional simulations for ethane adsorption would be useful for understanding the similarities and differences in these systems.

6. Conclusion

The multiple histogram reweighting technique has been used to study capillary condensation, prewetting transitions, and layering transitions. The critical capillary condensation temperature and density are estimated to be $T_c^* = 0.77$ and $\rho_c^* = 0.482$ for methane adsorption in a graphitic slit pore of width $H = 5\sigma$. Crossover of the effective exponent value from 2D Ising-like to mean-field occurs for capillary condensation. To our

knowledge, crossover for capillary condensation has not been observed previously. The precision and abundance of the coexistence data generated from MHR were crucial factors in the successful observation of crossover. Adsorption of Ar on solid CO₂ using the potential models of Finn and Monson shows prewetting transitions at temperatures lower than previously observed. The reduced wetting temperature is estimated to be around 0.69 from the extrapolation of the prewetting transition line and the saturated vapour line. The reduced critical prewetting temperature is about 0.92, as estimated from the disappearance of two distinct peaks in the density probability distribution. Layering transitions were computed from MHR for propane adsorbing on graphite. The transition pressures are in good agreement with previous simulations for larger system sizes, indicating that MHR calculations for small system sizes can be useful for predicting the behaviour of larger systems. We estimate $T_c(2) \sim 120$ K, based on the merging of the density probability distributions.

We have demonstrated that MHR can be a useful tool for computing the properties of adsorbed fluids, especially when one is interested in investigating phase transitions. However, there are drawbacks to MHR that should be mentioned. Efficiency in collecting histograms decreases dramatically with decreasing temperature and increasing volume. It is advisable to use the smallest simulation box size that is possible when performing MHR. The reason for this is twofold. (1) The overlap between neighbouring states becomes smaller as the system size increases, necessitating a larger number of simulations to span the same temperature range. (2) Longer simulations are required to capture the increased number of microstates available in larger systems. We have used standard Metropolis Monte Carlo in our work. Efficiency gains could be made by implementing biasing methods that would increase the width of the density and energy distributions sampled in a single simulation. However, it is clear that MHR is not a very efficient method if large system sizes are needed. Another drawback of the MHR method is that there is no clear way to estimate the precise critical temperature for a transition without resorting to finite-size scaling methods. The disappearance of two peaks in the density distribution is a sufficient but not necessary condition for a system being in the supercritical region. The double-peaked distribution is known to persist to temperatures that are slightly supercritical [58], so that absence of the two peaks can serve only as an upper bound measure of the critical point.

We thank Jeffrey Potoff for helpful discussions. This work was supported by the National Energy Tech-

nology Center and the National Science Foundation through CAREER Grant #CTS-9702239. Calculations were performed at the University of Pittsburgh Center for Molecular and Materials Simulations and the National Energy Technology Laboratory.

References

- [1] CHARVOLIN, J., JOANNY, J. F., and ZINN JUSTIN, J., 1988, *Liquids at Interfaces* (Amsterdam: North Holland).
- [2] TAUB, H., TORZO, G., LAUTER, H. J., and FAIN JR., S. C., 1991, *Phase Transitions in Surface Films*, Vol. 2 (New York: Plenum Press).
- [3] GELB, L. D., and GUBBINS, K. E., 1999, *Rep. Progr. Phys.*, **62**, 1573.
- [4] PETERSON, B. K., and GUBBINS, K. E., 1987, *Molec. Phys.*, **62**, 215.
- [5] JIANG, S. Y., RHYKERD, C. L., and GUBBINS, K. E., 1993, *Molec. Phys.*, **79**, 373.
- [6] PANAGIOTOPOULOS, A. Z., 1987, *Molec. Phys.*, **62**, 701.
- [7] CURTAROLO, S., STAN, G., COLE, M. W., BOJAN, M. J., and STEELE, W. A., 1999, *Phys. Rev. E*, **59**, 4402.
- [8] FINN, J. E., and MONSON, P. A., *Phys. Rev. A*, **39**, 6402.
- [9] FERRENBURG, A. M., and SWENDSEN, R. H., 1988, *Phys. Rev. Lett.*, **61**, 2635.
- [10] FERRENBURG, A. M., and SWENDSEN, R. H., 1989, *Phys. Rev. Lett.*, **63**, 1195.
- [11] FERRENBURG, A. M., and SWENDSEN, R. H., 1989, *Comput. Phys.*, **Sept/Oct**, 101.
- [12] DE PABLO, J. J., YAN, Q. L., and ESCOBEDO, F. A., 1999, *Ann. Rev. phys. Chem.*, **50**, 377.
- [13] PANAGIOTOPOULOS, A. Z., 2000, *J. Phys. Condens. Matter*, **12**, R25.
- [14] ESCOBEDO, F. A., 2000, *J. chem. Phys.*, **113**, 8444.
- [15] POTOFF, J. J., and SIEPMANN, J. I., 2001, *AIChE J.*, **47**, 1676.
- [16] GELB, L. D., and GUBBINS, K. E., 1997, *Physica A*, **244**, 112.
- [17] ESCOBEDO, F. A., and DE PABLO, J. J., 1999, *Phys. Rep.*, **318**, 85.
- [18] POTOFF, J. J., and SIEPMANN, J. I., 2000, *Phys. Rev. Lett.*, **85**, 3460.
- [19] LASTOSKI, C., and GUBBINS, K. E., 1993, *Langmuir*, **9**, 2693.
- [20] GELB, L. D., and GUBBINS, K. E., 1999, *Phys. Rev. Lett.*, **62**, 1573.
- [21] HEFFELFINGER, G. S., VAN SWOL, F., and GUBBINS, K. E., 1987, *Molec. Phys.*, **61**, 1381.
- [22] CAHN, J. W., 1977, *J. chem. Phys.*, **66**, 3667.
- [23] EBNER, C., and SAAM, W. F., 1977, *Phys. Rev. Lett.*, **38**, 1486.
- [24] BONN, D., and ROSS, D., 2001, *Rep. Progr. Phys.*, **64**, 1085.
- [25] SCHICK, M., 1988, *Liquids at Interfaces*, edited by J. Charvolin, J. F. Joanny, and J. Zinn Justin (Amsterdam: North Holland) p. 415.
- [26] FAN, Y., and MONSON, P. A., 1993, *J. chem. Phys.*, **99**, 6897.
- [27] MISTURA, G., ANCILOTTO, F., BRUSCHI, L., and TOIGO, F., 1999, *Phys. Rev. Lett.*, **82**, 795.
- [28] COLE, M. W., 1995, *J. low Temp. Phys.*, **101**, 25 and references therein.
- [29] COLE, M. W., 1998, *Fluid Phase Equilibria*, **151**, 559 and references therein.

- [30] YOUNG, H. S., MENG, X. F., and HESS, G. B., 1993, *Phys. Rev. B*, **48**, 14556.
- [31] HESS, G. B., 1991, *Phase Transitions in Surface Films*, Vol. 2, edited by H. Taub, G. Torzo, H. J. Lauter and S. C. Fain Jr. (New York: Plenum Press) p. 357.
- [32] IWAMATSU, M., 1998 *J. Colloid Interface Sci.*, **199**, 177.
- [33] ZHANG, Q. M., FENG, Y. P., KIM, H. K., and CHAN, M. H. W., 1986, *Phys. Rev. Lett.*, **57**, 1456.
- [34] RAMESH, S., ZHANG, G., TORZO, G., and MAYNARD, J. D., 1984, *Phys. Rev. Lett.*, **52**, 2375.
- [35] SHI, W., and JOHNSON, J. K., 2001, *Fluid Phase Equilibria*, **187–188**, 171.
- [36] STEELE, W. A., 1973, *Surface Sci.*, **36**, 317.
- [37] STEELE, W. A., 1974, *The Interaction of Gases with Solid Surfaces* (Oxford: Pergamon Press).
- [38] SMIT, B., 1992, *J. chem. Phys.*, **96**, 8639.
- [39] DILLMANN, O., JANKE, W., MÜLLER, M., and BINDER, K., 2001, *J. chem. Phys.*, **114**, 5853.
- [40] MON, K. K., and BINDER, K., 1992, *J. chem. Phys.*, **96**, 6989.
- [41] FINN, J. E., and MONSON, P. A. 1990, *Phys. Rev. A*, **42**, 2458.
- [42] NEIMARK, A. V., and RAVIKOVITCH, P. I., 1997, *Langmuir*, **13**, 5148.
- [43] TALU, O., and MYERS, A. L., 2001, *AIChE J.*, **47**, 1160.
- [44] SIRCAR, S., 2001, *AIChE J.*, **47**, 1169.
- [45] HILL, T. L., 1963, *Thermodynamics of Small Systems*, Part I (New York: Benjamin).
- [46] ANCILOTTO, F., and TOIGO, F., 1999, *Phys. Rev. B*, **60**, 9019.
- [47] MISTURA, G., LEE, H. C., and CHAN, M. H. W., 1994, *J. low Temp. Phys.*, **96**, 221.
- [48] TELETZKE, G. F., SCRIVEN, L. E., and DAVIS, H. T., 1982, *J. Colloid Interface Sci.*, **87**, 550.
- [49] TARAZONA, P., and EVANS, R., 1983, *Molec. Phys.*, **48**, 799.
- [50] HAUGE, E. H., and SCHICK, M., 1983, *Phys. Rev. B*, **27**, 4288.
- [51] LUSTIG, R., and STEELE, W. A., 1988, *Molec. Phys.*, **65**, 475.
- [52] JORGENSEN, W. L., MADURA, J. D., and SWENSON, C. J., 1984, *J. Amer. chem. Soc.*, **106**, 813.
- [53] MARTIN, M. G., and SIEPMANN, J. I., 1998, *J. phys. Chem. B*, **102**, 2569.
- [54] NATH, S. K., ESCOBEDO, F. A., and DE PABLO, J. J., 1998, *J. chem. Phys.*, **108**, 9905.
- [55] SIEPMANN, J. I., KARABORN, S., and SMIT, B., 1993, *Nature*, **365**, 330.
- [56] ZHAO, X., KWON, S., VIDIC, R. D., BORGUET, E., and JOHNSON, J. K., 2002, submitted.
- [57] JIANG, S. Y., ZOLLWEG, J. A., and GUBBINS, K. E., 1993, *Molec. Phys.*, **83**, 103.
- [58] POTOFF, J. J., private communication.
- [59] NHAM, H. S., and HESS, G. B., 1988, *Phys. Rev. B*, **38**, 5166.
- [60] TARAZONA, P., and EVANS, R., 1983, *Phys. Rev. A*, **28**, 1864.
- [61] MEISTER, T. F., and KROLL, D. M., 1985, *Phys. Rev. A*, **31**, 4055.
- [62] SOKOŁOWSKI, S., and FISCHER, J., 1990, *Phys. Rev. A*, **41**, 6866.
- [63] BOJAN, M. J., STAN, G., CURTAROLO, S., STEELE, W. A., and COLE, M. W., 1999, *Phys. Rev. E*, **59**, 864.